PCCP

Character Angle Effects on Dissociated Dislocation Core Energy in Aluminum

Journal:	*Physical Chemistry Chemical Physics*
Manuscript ID	CP-ART-10-2020-005333.R1
Article Type:	Paper
Date Submitted by the Author:	16-Dec-2020
Complete List of Authors:	Zhou, Xiao Wang; Sandia National Laboratories, Foster, Michael; Sandia National Laboratories, Materials Chemistry

Character Angle Effects on Dissociated Dislocation Core Energy in Aluminum

X. W. Zhou, and M. E. Foster

Mechanics of Materials Department, Sandia National Laboratories, Livermore, California 94550, USA, Email: xzhou@sandia.gov

ABSTRACT

Dislocation core energy is an important property in materials mechanics but can only be obtained from atomistic simulations. Periodic boundary conditions are ideally suited for atomistic calculations of dislocation energies but have faced two major challenges. First, viable methods to extract core energies from atomistic data of total energies have been developed only for non-dissociated dislocations whereas realistic dislocations are often dissociated into partials. Second, core energy is a function of dislocation character angle. This functional dependence can only be revealed through calculations at a variety of character angles. This requires both additional computational resources and a robust method to implement arbitrary character angles. Here a new procedure has been developed to overcome both challenges. By applying this approach, we have calculated 22 core energies of dissociated dislocations in aluminium over the entire character angle range between 0^o and 90^o. In addition to the discrete core energy data for dissociated dislocations, we found that core energy can be approximated by a continuous function of character angle. Specifically, our dissociated dislocation core energies have been well fitted to a polynomial Sinoidal function of character angle. We have also discovered that there exists a critical system dimension below which dislocation core energies cannot be calculated due to dislocation transformation.

PACS number(s): 61.72.Lk, 02.70.Ns, 61.72.Bb

Keywords: molecular dynamics, dislocation core energy, aluminium

I. INTRODUCTION

All sophisticated plastic deformation and fracture behaviour of materials can ultimately be attributed to dislocation migration. As a result, dislocation core energy E_c is an important input parameter for studying mechanical performance of materials using mesoscale modelling methods such as dislocation dynamics [1]. This is because E_c contributes to the dislocation line tension, which determines the behaviour of dislocation lines as they bow out to bypass obstacles and react to form junctions. Because dislocation cores cannot be described by linear elasticity theory, E_c must be calculated from atomistic simulations.

To incorporate the long-range elastic field of dislocations in bulk materials, atomistic calculations of dislocation core energies usually use either continuum [2,3,4,5,6] or periodic [1,7,8,9,10,11,12,13,14] boundary conditions. Under the continuum boundary conditions, only a region close to the dislocation core is treated with atomistic simulations whereas atoms far away from the core are fixed at the locations determined from continuum solution of the dislocation strain field. This method necessarily involves approximations. For example, continuum solution of dislocation strain field must assume a dislocation type whereas relaxed dislocations are always composed of partial dislocations separated by stacking faults whose configurations are unknown *a priori*. Furthermore, the fixed region must be simulated at zero temperature. Of course, the definition and dimension of the core and boundary regions incur additional subjective choices. On top of these challenges, the continuum boundary method is not easy to apply because the continuum solution of dislocation elastic strain field requires the use of an anisotropic elastic theory where a full set of elastic constants defined by the same interatomic potential need to be

used as inputs. These elastic constants can only be obtained through independent set of atomistic simulations.

Simulations with periodic boundary conditions do not involve the approximations described above. For example, periodic boundary conditions allow dislocation cores to self-consistently evolve during the simulation. Although the periodic boundary conditions cause "a" dislocation to become a dislocation array, this does not affect the result because the core energy of a given dislocation type can be treated as a constant that is independent of the number of dislocations considered.

Past calculations of dislocation core energies using the periodic boundary conditions have faced two major challenges. First, dislocation energy can be easily calculated as the energy difference between systems with and without dislocations under the condition that both systems have the same number of atoms. The total dislocation energy, however, needs to be fit to a linear elastic continuum model to extract the core energy. Such a continuum model has only been developed for non-dissociated dislocations [15,16] whereas in reality dislocations are most likely dissociated into partials. Resolving partial dislocations in mesoscale models is needed to understand the effects of stacking fault width which seems to impact deformation behavior of some materials (e.g., austenitic stainless steels [17]). Second, dislocation core energy E_c changes with the character angle β formed between the dislocation line and the Burgers vector. To identify the relationship between E_c and β, the atomistic simulation method used to calculate dislocation energies must be applied to a variety of character angles spanning the entire range between 0^o and 90^o. In addition, the calculated results must have negligible errors for large systems. These requirements impose some difficulties to the atomistic calculations.

The objective of the present work is fourfold. First, we give a brief overview of the literature periodic methods. Next, we develop a new periodic method that can be easily applied to arbitrary character angles. We then demonstrate a new procedure that enable atomistic simulation results to be fit to a linear elastic theory with dissociated dislocations. Finally, we explore effects of system dimensions on calculated dislocation core energies. As an example, we will look at face-centred-cubic (fcc) aluminum using the Al-Cu bond order potential (BOP) [18], where core energies have already been calculated for non-dissociated dislocations [15].

II. OVERVIEW OF THE PERIODIC BOUNDARY METHOD

Historically, the periodic boundary method was implemented using a so-called quadruple dislocation configuration [10] as shown in Figs. 1(a) and 1(b). Here, positive and negative dislocations (lying in z) alternate in sign in both x and y directions, so that a negative dislocation can recover the crystal periodicity destroyed by the preceding positive dislocation. The initial implementation of the quadruple dislocation configuration requires four dislocations per orthogonal computational cell. This is shown in Fig. 1(a) where the red dash frame shows a computational cell with all dislocations at the cell boundaries to reveal the periodicity; and the red solid frame shows the translated cell with all the dislocations inside the cell. A potential issue with this implementation is that, the positive and negative dislocations are on the same slip plane (x-z), so they can glide and annihilate. The quadruple model has been widely used as shown by its extensive citation including references [11,12]. It is interesting to note that the quadruple configuration can be replicated with a non-orthogonal cell containing only two dislocations [10]. This is illustrated in Fig. 1(b) where similar dash and solid frames again reveal the periodicity and number of dislocations per cell respectively. Interestingly, literature attributes the advantage of this non-orthogonal cell to its improved computational efficiency due to the 50% reduction in

the total number of atoms [10]. However, it is worth noting that in Fig. 1(b), the two positive (or equivalently negative) dislocations along the tilted y direction are the same image dislocation so that the glide of the positive and negative dislocations along the x direction is constrained, making them more difficult to migrate towards each other and annihilate. For instance, the easiest annihilation mechanism in Fig. 1(a) is that a vertical dipole approaches its neighbouring vertical dipole. In Fig. 1(b), however, a vertical dipole can never approach its periodic image.

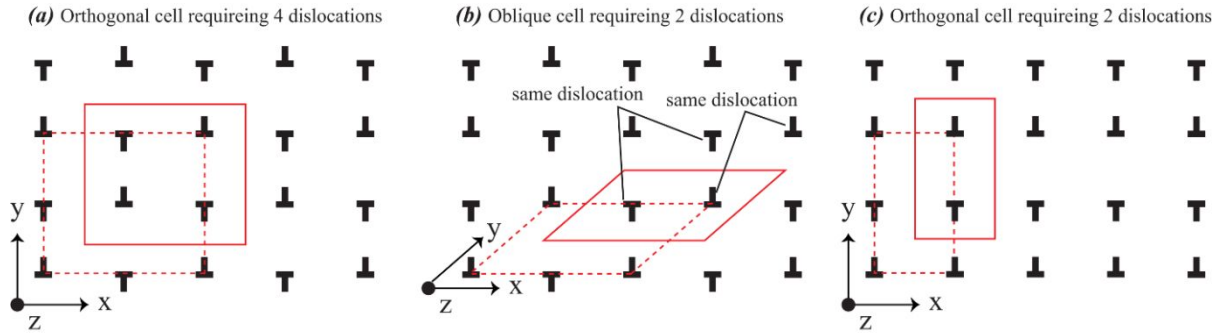

Fig. 1. Schematic of dislocation configurations: (a) quadruple dislocations using an orthogonal cell; (b) quadruple dislocations using an oblique cell; and (c) dipole dislocations using an orthogonal cell.

The quadruple approach was primarily used in early days for computational efficiency reasons. On the other hand, seriously oblique computational cells can result in slightly increased computations because atom's neighbours in oblique cells can be located many periodic images away. To eliminate the use of an oblique computational cell and to completely prevent the annihilation of positive and negative dislocations along the x direction, the alternation of dislocation sign in the x direction under the periodic boundary condition can be removed, leaving only one periodic dislocation dipole in the y direction as illustrated in Fig. 1(c). As will be shown below, the correct periodic boundary conditions for mixed dislocations can be rigorously generated for this configuration.

Cai et al [7,8,9] have developed an approach to use non-orthogonal cell to create a general dislocation dipole under periodic boundary conditions. As pointed out above, the total dislocation energies obtained from atomistic simulations need to be fitted to a continuum prediction of the same energies using the same geometry to extract the core energy. Cai et al found that in the geometry they used, such a continuum prediction could not be expressed analytically due to a conditional divergence problem [7,19]. Regardless, the numerous successful dislocation core energy calculations reported by Cai et al are encouraging.

It is interesting to point out that the atomistic simulations cited above primarily use molecular statics (MS) energy minimization. When systems contain dislocations, MS simulations may converge to an unintended local energy minimum state, resulting in error in the calculated dislocation energies [20]. Contrary to intuition, such an error can be unacceptably large for large systems, which has been explicitly demonstrated for an exemplar zinc-blende model compound CdS [21]. This problem is mitigated when relatively small system sizes are used.

Recently, we reported calculations of dislocation core energies in aluminium at some selected character angles [15,16]. Our work distinguished from earlier literature calculations in several ways. First, we used orthogonal computational cell where the periodic boundary conditions were ensured by increasing the number of dislocations per cell albeit with the same dislocation array as shown in Fig. 1(c). Second, we derived an analytical expression for non-dissociated dislocation energies from continuum theory. This enabled the dislocation core energy to be extracted by direct fitting to the atomistic dislocation energies. Importantly, we used time-averaged molecular dynamics (MD) instead of MS to calculate the energies, which virtually removed the error in the calculations regardless of system size (this seems to be counterintuitive because a snapshot of an MD result, taken at any given time, does involve significant thermal

noise). However, our previous method is associated with a technical difficulty: for the non-regular character angles that we studied, such as $\beta = 10.89^o$, 19.11^o, 40.89^o, 49.11^o, 70.89^o, 79.11^o, we had to use 56 dislocations per cell to ensure the periodicity. Other non-regular character angles may easily require far more dislocations. This effectively limited our calculations of dislocation core energies to only 10 different dislocation character angles with $\sim 10^o$ interval for the entire character angle range (0^o - 90^o), which may not be sufficient to determine confidently the continuity of the E_c vs. β function. It is also difficult for other researchers to follow our method. In addition, our previous approach is only valid at $d = L_y/2$ [15], where d and L_y are dipole distance and system dimension in y respectively, as marked in Fig. 2. For a given dislocation type, the core energy is a constant whereas the dislocation elastic energy outside of the core depends on both vertical and horizontal dislocation spacings d and S (see Fig. 2). This means that the elastic energy outside of the core can be more accurately identified by fitting dislocation energies at various d and S rather than dislocation energies at various S only. In fact, the dependence of dislocation energy on the vertical spacing d is more interesting than on the horizontal spacing S. First, increasing S means increasing system dimension and hence the computational cost, whereas increasing d under fixed L_y does not change system dimension. Second, the elastic energy of the dislocation is more sensitive to d than to S. Specifically, as will be shown below, dislocation energy is a symmetric function of d, with the maximum energy occurring at $d = L_y/2$, and near zero energy occurring at $d \rightarrow 0$ or $d \rightarrow L_y$. This provides a strong validation of the MD results. Hence, the inability of the previous method to address different vertical spacings is undesired. Finally, because we introduced 28 dipoles (56 dislocations), the dislocation spacing, S, can become small (although because our system dimensions L_x and L_y are extremely large, our dislocation spacing $S = L_x/28$ may still be

above many literature calculations). In the next section, we develop a new approach that ensures periodicity with only one dislocation dipole per cell, and yet allows any values of character angle $\beta > 0^o$ and vertical spacing d. Our method is general as we focus on the periodicity of the discrete nature of the lattice. Note that our method differs from the one used by Cai et al [7,8,9]; they introduce a dislocation dipole by displacing atoms according to continuum displacement fields.

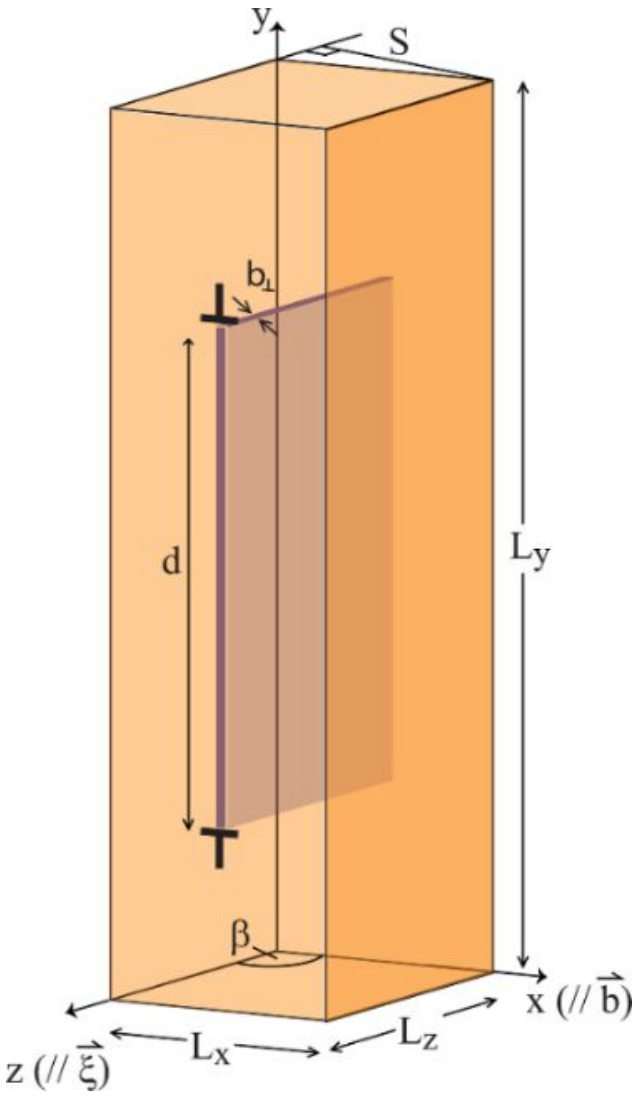

Fig. 2. Schematic of computational cell with the x-axis parallel to the Burgers vector $\vec{b}$, the z-axis parallel to dislocation line vector $\vec{\xi}$, and the y-axis perpendicular to both x and z.

III. NEW PERIODIC BOUNDARY METHOD

The concept of our atomistic method is general and can be applied to many different dislocations including those that are not on the slip plane, and many different crystal structures including fcc, body-centred-cubic (bcc), and hexagonally-closely packed (hcp) structures. A schematic of our computational cell is shown in Fig. 2. The key to ensure the periodic boundary conditions after adding only one dislocation dipole with any arbitrary character angle β is to use a computational cell where the two axes (x and z) on the dislocation slip plane are not orthogonal but rather form the dislocation character angle β; the third axis (y) is still orthogonal to the slip plane. This allows the Burgers vector $\vec{b}$ to be aligned with one of the slip plane axes (e.g., x), and dislocation line vector $\vec{\xi}$ with the other slip plane axis (z). To add a dislocation dipole, a layer of material with a thickness of $b_\perp$ is removed as shown in Fig. 2, where $b_\perp$ is the magnitude of the edge component of the Burgers vector. If b is the magnitude of the total Burgers vector, $b_\perp = b \sin\beta$. The atoms near the removed atoms are then dilated towards the gap by ±b/2 along the Burgers vector direction $\vec{b}$ (i.e., the x-axis) so that the gap is closed. This process creates a dislocation dipole with a character angle β but makes no changes to the stacking of atoms on the boundaries of the computational cell. As a result, the periodic boundary conditions remain intact. In the geometry shown in Fig. 2, we assume that the system has dimensions of L_x, L_y, and L_z, the dislocation spacing S on the slip plane equals $L_x \sin\beta$, and the dislocation spacing d along the y direction equals the height of the missing planes.

This process is applicable for any character angle β except for screw dislocation where $\beta = 0^o$. This is acceptable because screw dislocation can be easily modelled using the previous method [15]. However, for any non-screw dislocation with $\beta \rightarrow 0^o$, the computational cell is extremely oblique. As discussed above, this is not desired for computational efficiency. It should also be recognized that the dynamic response of the barostatting algorithms used in MD

simulations are affected by the skewness of the computational cell. As a result, we use three approaches to improve the orthogonality of the cell.

First, assume that we have an oblique cell as indicated by the thick dash lines in Fig. 3(a). Without affecting the periodic boundary conditions, we can reduce the obliqueness by translating one edge of the cell along the z-axis an integer number of times of the periodic length L_z, as indicated sequentially by thin red, thin blue, thin green, and thick black lines. The thick black cell has the minimum obliqueness because further translating the cell will start to increase the obliqueness. This minimum obliqueness is quantified by the distance xz in Fig. 3(a), which measures the deviation of the cell from an orthogonal reference.

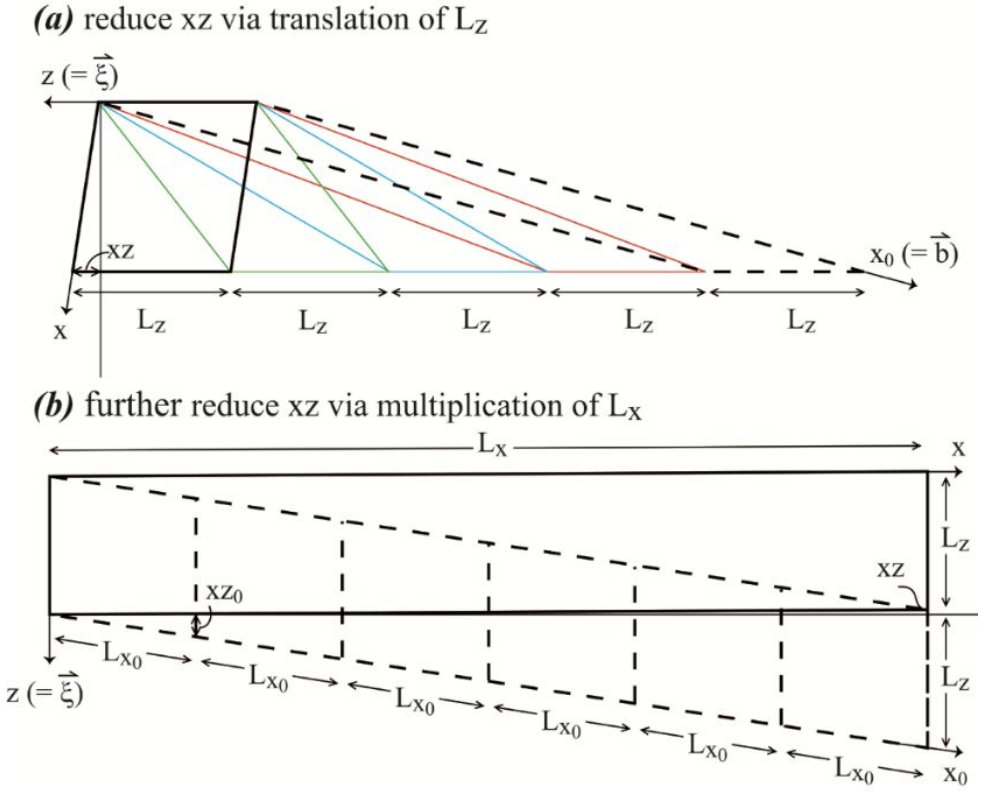

Fig. 3. Schematic of procedures to reduce cell obliqueness: (a) effects of translating the cell edge in the z direction; (b) effects of increasing the length in the x direction.

Second, it can be seen from Fig. 3(a) that a smaller xz is likely to be obtained if the periodic cell dimension L_z is smaller. Hence, we always use the smallest L_z possible with the crystal periodicity to create an initial crystal cell, recognizing that when the near-orthogonal cell as shown by the thick black frame in Fig. 3(a) is finalized, L_z can be periodically expanded to approach a desired value.

Third, we can further reduce the obliqueness of the cell by increasing the length along the x-axis as shown in Fig. 3(b). Assume that the original x-axis is notated as x_0 and periodic length along x_0 is L_{x0}, the periodic boundary conditions will remain intact if the length increase is a multiple of L_{x0}. Once the length in x_0 is appropriately increased, subsequent translation in z using the approach described in Fig. 3(a) can give any desired small obliqueness for the transformed x-axis. Fig. 3(b) compares the final obliqueness, xz, with the obliqueness, xz_0, prior to the increase of the x dimension. The increased x dimension is now denoted as L_x.

Trial-and-error was used to decide our system dimensions that give a small obliqueness. All our simulations used a y dimension of $L_y \sim 407$ Å except for the $\beta = 0^o$ case where a large $L_y \sim 1220$ Å was used to avoid cross slip that may occur due to the attraction between two opposite screw dislocations. Various dimensions corresponding to horizontal dislocation spacing S between 43 and 700 Å were used in the x direction, and various dimensions corresponding to dislocation line length between 23 and 64 Å were used in the z direction. As an example, some calculations for $\beta = 81.052^o$ used large systems (e.g., ~350×407×55 $Å^3$ volume and ~500,000 atoms). Note that the dislocation line length does not affect the results, and the use of statistically different line lengths is only for a sanity check. As will be shown below, the minimum dislocation spacing $S \geq 43$ Å is important as core energies may be incorrect at smaller spacings.

IV. CONTINUUM EXPRESSION OF DISSOCIATED DISLOCTION ENERGY

Under periodic boundary conditions, dissociated dislocation energy should be a function of geometry and property parameters. Geometry parameters include horizontal and vertical periodic spacings (S and L_y) between dipoles, dipole distance (d), and stacking fault width (λ). Property parameters include core energy and core radius (E_c and r_0), shear modulus and Poisson's ratio (G and ν), Burgers magnitude and dislocation character angle (b and β), and stacking fault energy (γ_{sf}). Continuum expression of the energy of dissociated dislocation (sum for both partials) on these parameters has only been derived recently from isotropic linear elastic theory [22]:

$$\Gamma = \begin{cases} E_c + \dfrac{Gb^2 sin^2\beta}{4\pi(1-\nu)} ln\dfrac{1}{r_0} + \dfrac{Gb^2 sin^2\beta}{4\pi(1-\nu)}[c_{ue0}(d) + c_{ue}(d)] + \\ \dfrac{Gb^2 cos^2\beta}{4\pi} ln\dfrac{1}{r_0} + \dfrac{Gb^2 cos^2\beta}{4\pi}[c_{us0}(d) + c_{us}(d)] + \Delta E_{dis} \end{cases} \quad (1)$$

where E_c is the total core energy of the dissociated dislocation (i.e., including two partials), b and β take the values of the perfect dislocation, ΔE_{dis} is dissociation energy, and functions $c_{ue0}(d)$, $c_{us0}(d)$, $c_{ue}(d)$, $c_{us}(d)$ are expressed as

$$c_{ue0}(d) = ln\left[\frac{(L_y - d)d}{L_y}\right] - ln\left[Ga\left(\frac{L_y + d}{L_y}\right)\right] - ln\left[Ga\left(2 - \frac{d}{L_y}\right)\right] \quad (2)$$

$$c_{us0}(d) = ln\left[\frac{(L_y - d)d}{L_y}\right] - ln\left[Ga\left(\frac{L_y + d}{L_y}\right)\right] - ln\left[Ga\left(2 - \frac{d}{L_y}\right)\right] \quad (3)$$

$$c_{ue}(d) = \sum_{i=1}^{\infty} \left\{ \begin{array}{l} \dfrac{4\pi \cdot i \cdot S \cdot coth\left(\dfrac{\pi \cdot i \cdot S}{L_y}\right) \cdot sin^2\left(\dfrac{\pi d}{L_y}\right)}{L_y cosh\left(\dfrac{2\pi \cdot i \cdot S}{L_y}\right) - L_y \cdot cos\left(\dfrac{2\pi d}{L_y}\right)} + \\ ln\left[cos^2\left(\dfrac{\pi d}{L_y}\right) + coth^2\left(\dfrac{\pi \cdot i \cdot S}{L_y}\right) \cdot sin^2\left(\dfrac{\pi d}{L_y}\right)\right] \end{array} \right\} \quad (4)$$

$$c_{us}(d) = \sum_{i=1}^{\infty} ln\left[cos^2\left(\frac{\pi d}{L_y}\right) + coth^2\left(\frac{\pi \cdot i \cdot S}{L_y}\right) \cdot sin^2\left(\frac{\pi d}{L_y}\right)\right] \quad (5)$$

In Eqs. (2) – (5), Ga() is an Euler gamma function, coth() and cosh() are hyperbolic functions.

The dissociation energy is calculated as

$$\Delta E_{dis}(\lambda) = -\left[w(\lambda) - w(r_0)\right] \tag{6}$$

with the function w(x) defined as

$$w(x) = w_{row}(x,y=0) + \sum_{i=1}^{\infty}\begin{Bmatrix} w_{col}[(i-1)\cdot S + S/2,(i-1)\cdot S + x, y \neq 0] + \\ w_{col}\left[-i\cdot S + \frac{S}{2}, -i\cdot S + x, y \neq 0\right] \end{Bmatrix} \tag{7}$$

where

$$w_{row}(x,y=0) = \frac{Gb^2[1-2cos(2\beta)]}{48\pi(1-\nu)}\mathrm{c}_{e0}(x) + \frac{Gb^2[1+2cos(2\beta)]}{48\pi}\,\mathrm{c}_{s0}(x) \tag{8}$$

$$w_{col}(x_1,x_2,y\neq 0) = \begin{cases} \frac{Gb^2[1-2cos(2\beta)]}{48\pi(1-\nu)}\left[\mathrm{c}_{3e,1}(x_1,x_2) + \mathrm{c}_{3e,2}(x_1,x_2)\right] + \\ \frac{Gb^2[1+2cos(2\beta)]}{48\pi}\,\mathrm{c}_{3s}(x_1,x_2) \end{cases} \tag{9}$$

In Eqs. (8) and (9), functions $c_{e0}(x)$, $c_{s0}(x)$, $c_{3e,1}(x_1,x_2)$, $c_{3s}(x_1,x_2)$, $c_{3e,2}(x_1,x_2)$ are defined as

$$\mathrm{c}_{e0}(x) = \mathrm{c}_{s0}(x) = 2ln\prod_{i=1}^{\infty}\left[\frac{(i-1)S + x}{(i-1)S + S/2}\cdot\frac{-i\cdot S + x}{-i\cdot S + S/2}\right] = ln\left[sin^2\left(\frac{\pi x}{S}\right)\right] \tag{10}$$

$$\begin{aligned} &\mathrm{c}_{3e,1}(x_1,x_2) = \mathrm{c}_{3s}(x_1,x_2) = ln\left(\frac{d^2+x_1^2}{d^2+x_2^2}\right) + \\ &ln\prod_{i=1}^{\infty}\left[\frac{x_2^2+(i\cdot L_y)^2}{x_1^2+(i\cdot L_y)^2}\cdot\frac{x_1^2+(i\cdot L_y-d)^2}{x_2^2+(i\cdot L_y-d)^2}\cdot\frac{x_2^2+(i\cdot L_y)^2}{x_1^2+(i\cdot L_y)^2}\cdot\frac{x_1^2+(i\cdot L_y+d)^2}{x_2^2+(i\cdot L_y+d)^2}\right] \end{aligned} \tag{11}$$

$$c_{3e,2}(x_1,x_2) = \frac{2d^2}{d^2+x_1^2} - \frac{2d^2}{d^2+x_2^2} + \sum_{i=1}^{\infty}\left[\begin{array}{l} -\frac{4(i\cdot L_y)^2}{x_1^2+(i\cdot L_y)^2} + \frac{2(i\cdot L_y-d)^2}{x_1^2+(i\cdot L_y-d)^2} + \frac{2(i\cdot L_y+d)^2}{x_1^2+(i\cdot L_y+d)^2} + \\ \frac{4(i\cdot L_y)^2}{x_2^2+(i\cdot L_y)^2} - \frac{2(i\cdot L_y-d)^2}{x_2^2+(i\cdot L_y-d)^2} - \frac{2(i\cdot L_y+d)^2}{x_2^2+(i\cdot L_y+d)^2} \end{array}\right] \quad (12)$$

Although no closed-forms have been found for Eqs. (4), (5), (11) and (12), these equations converge rapidly []. In this work, we take 100 terms in the summation so that error is essentially zero in our calculations. Note that Eqs. (1) – (12) are only applicable to planar dislocation core structures in isotropic systems. For example, they can be used for non-screw dislocations in bcc crystals; however, they are not applicable for non-planar screw dislocations typically seen in bcc crystals.

V. VALIDATION OF MD DISLOCATION ENERGIES

Our simulations were performed using the MD code LAMMPS [23,24]. To prevent dislocation migration from initial locations, centres of mass for small regions immediately above and below the slip plane near the dislocation core are fixed using the "fix … recenter" command (note that the "fix … momentum" command is not good enough). Since only centres of mass are fixed but atoms are still free to move, this constraint does not impact dislocation core structures whose relaxation is symmetric about the core centre. The "error-free", time-averaged MD method was used to calculate dislocation energies [15]. All MD simulations were performed at 300 K for 4.0 ns using a zero pressure NPT (constant number of atoms, pressure, and temperature) ensemble. The first 0.8 ns simulations were discarded to enable the system to reach an equilibrium. Time-averaged energies were calculated for the remaining 3.2 ns. These averaged energies were used to calculate the dislocation energies.

22 character angles $\beta = 0.00^o$, 6.59^o, 8.95^o, 10.89^o, 19.11^o, 21.05^o, 23.41^o, 30.00^o, 36.59^o, 38.95^o, 40.89^o, 49.10^o, $51^o.05^o$, 53.41^o, 60.00^o, 66.59^o, 68.95^o, 70.89^o, 79.11^o, 81.05^o, 83.41^o, 90.00^o were considered. For $\beta = 0.00^o$, the method proposed here cannot be used so we used the previous approach [15]. These 22 character angles involve 22 unknown core energies E_c. The previous work indicates that the isotropic elastic theory is enough to describe dislocation core energy of aluminium [15]. Given the isotropic elastic theory as described by Eq. (1), we have 26 more unknown parameters that include shear modulus G and Poisson's ratio ν, stacking fault energy γ_{sf}, dislocation core radius r_0, and 22 stacking fault widths λ at the 22 character angles. For perfect dislocations, dislocation core radius can be arbitrarily chosen as long as it is consistent with the core energy [15]. For dissociated dislocations, a small core radius should be used so that the dissociation energy ΔE_{dis} is not digested into the core energy and the model can resolve small stacking fault width. Here a small core radius of $r_0 = 0.2$ Å is used to ensure that the core radius does not significantly impact stacking fault width, i.e., $\lambda \approx \lambda - 2\, r_0$. Stacking fault widths are not independent parameters; they can be solved from the minimum energy condition $\partial\Gamma/\partial\lambda = 0$ using Eq. (1). Independent time-averaged MD simulations were performed to calculate the stacking fault energy, and $\gamma_{sf} = 0.0085$ eV/Å^2 was obtained at our simulated temperature 300 K. Hence, we only have 24 independent unknown parameters: 22 core energies plus G and ν. One minimum approach to parameterize these 24 unknowns is to fit three (total) dislocation energies at three dislocation spacings for one of the character angles, and one dislocation energy for each of the remaining character angles. However, our simulations were significantly more extensive than the minimum 24 cases. For each of the character angles $\beta \neq 0^o$, two series of dislocation energies were calculated. Referring to Fig. 2, one series explores different vertical dislocation spacings d, and the other series explores different horizontal dislocation spacings S.

For $\beta = 0^o$, only one series with respect S was performed because the approach works well only for $d = L_y/2$. This resulted in 184 total dislocation energies. The extensive data sets enable us to more accurately fit the elastic contribution as mentioned above and to validate the results. Specifically, dislocation energy as a function of the vertical dislocation spacing d is mirror symmetric at $d = L_y/2$. This is because under the periodic boundary conditions, if a dislocation is separated from a neighbouring dislocation by d, then it must be separated from an image neighbouring dislocation by $L_y - d$. Equal spacings to these two neighbours occur when $d = L_y/2$. Furthermore, dislocation energies drop to zero when $d = 0$ or $d = L_y$ where the two opposite dislocations annihilate. The relaxation scheme fails if the results do not strictly satisfy this symmetric condition. For instance, we found that the results obtained from energy minimization not only had large statistical uncertainty margin, but also did not rigorously satisfy the symmetric condition.

As one example, energies of dislocations at two character angles of $\beta = 30^o$ and $\beta = 60^o$ obtained from simulations are shown using the small blue data points in Fig. 4. Note that our time averaged calculations were output 100 times for smaller time segments and our final results were further averaged over these 100 values. The reason to get 100 values for smaller time segments is to evaluate the standard deviations of our final results as described previously [15], and these standard deviations are included in Fig. 4 as the error bars. Here Fig. 4(a) shows the effects of the vertical dislocation spacing d at a fixed horizontal spacing, $S = L_x \sim 44$, Å and a fixed y dimension, $L_y \sim 407$ Å, and Fig. 4(b) illustrates the effects of the horizontal dislocation spacing S at a fixed vertical dislocation spacing, $d = L_y/2 \sim 203.5$ Å. Further, the shaded regions in the figure represent the decrease of energy during dislocation dissociation (i.e., ΔE_{dis}). Both lines and shaded regions were calculated from continuum expressions [15] to be discussed

below. Fig. 4 indicates that all MD error bars are reduced to horizontal lines, meaning that error of the MD results is near "zero" on the scale of the figure. This level of accuracy cannot be achieved by MS simulations. A result of the near zero error is that all data points fall on smooth trends. Here by smooth trends we mean that the data points do not exhibit up-and-down type of statistical errors. This does not necessarily mean that the data points fall on the continuum lines, although in Fig. 4, there is a good agreement with the continuum lines. Interestingly, Fig. 4(a) shows that dislocation line energy is an ideally symmetric function of the vertical dislocation spacing, d, strongly validating the results as discussed above. This validation could not be done using the previous approach that is constrained at $d = L_y/2$ [15]. From Fig. 4, we see that dislocation dissociation energy ΔE_{dis} is not negligible.

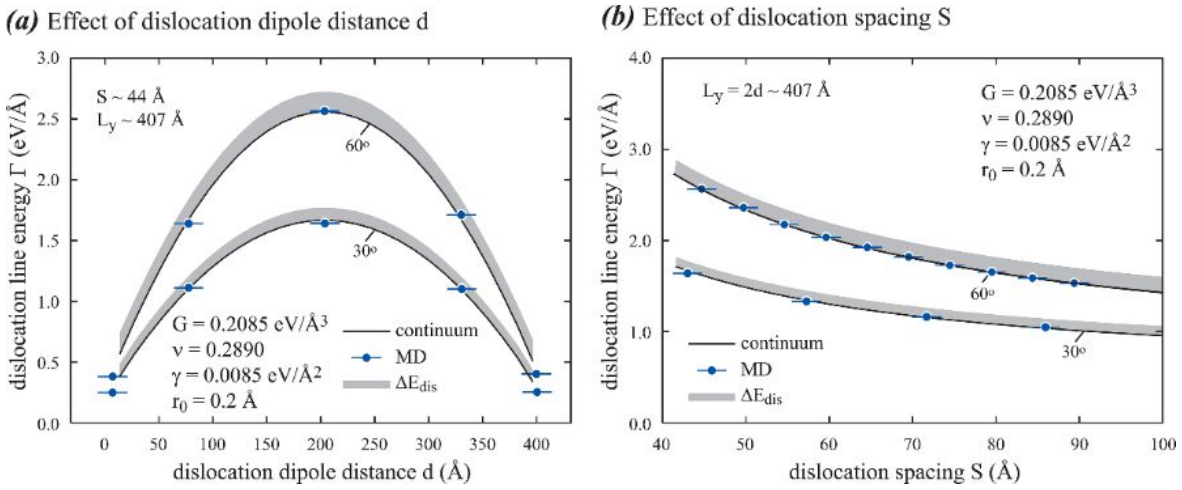

Fig. 4. Energies of $\beta = 30^o$ and $\beta = 60^o$ dislocations as a function of (a) vertical dislocation spacing d and (b) horizontal dislocation spacing S. Data points are from MD and curves are continuum fits. The horizontal bars of data points indicate negligible errors, and the shaded regions denote the decrease of energy due to dislocation dissociation (i.e., ΔE_{dis}).

A similar level of accuracy is achieved for all 22 character angles. Instead of showing many similar figures as already illustrated in Fig. 4, we compare all 184 MD dislocation energies with the continuum fits (to be described below) in Fig. 5. Here, the x-axis is MD dislocation energy

and y-axis is the corresponding continuum energy. Strictly speaking, not all data points in Fig. 5 fall exactly on the y = x line. Nonetheless, this is just a deviation of the continuum model from the MD data; and all the Γ vs. d and Γ vs. S MD data points (such as those shown in Fig. 4) still fall on smooth trends without up-and-down errors as can be seen in the supplemental material [25]. Fig. 5 clearly indicates that the deviation from the y = x line is small meaning that MD and continuum results are in good agreement. We point out again that the continuum expression can only fit 24 MD data points, and the good match for the remaining 160 data points strongly validate both the MD results and the continuum expression.

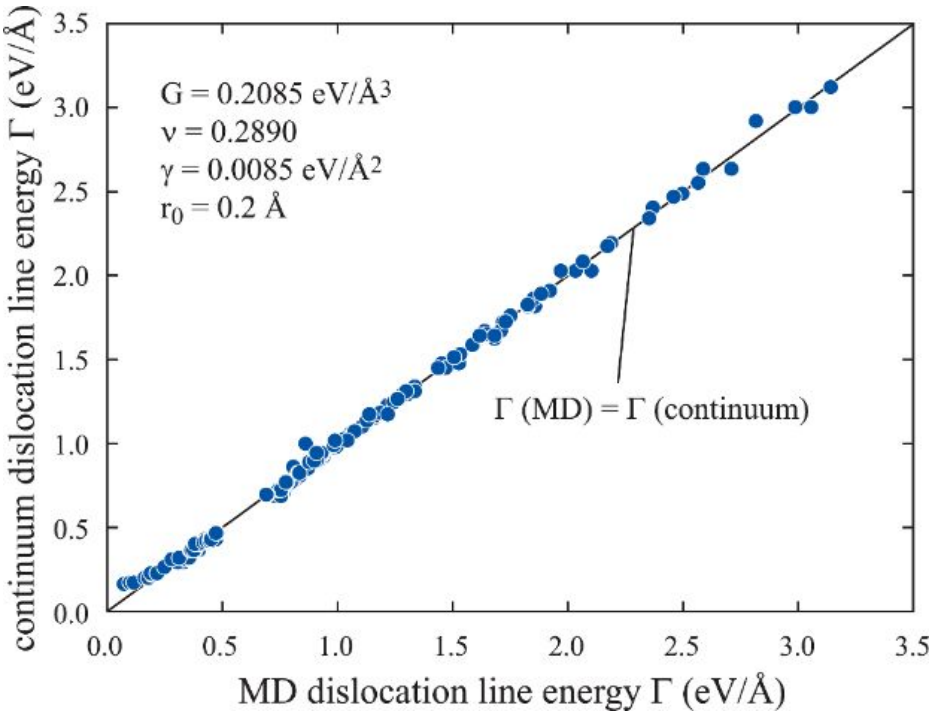

Fig. 5. Comparison of all MD and continuum dislocation energy results.

Quantitatively, the accuracy shown in Figs. 4 and 5 approximately corresponds to 1 eV margin in total energy of a million-atom system. This translates to < 0.000001 eV/atom, which cannot be achieved by any MS schemes. The error of time-averaged MD simulations, in principle, always decreases with time t following approximately the $t^{-1/2}$ scaling. More

interestingly, even numerical truncation errors can be averaged out if we assume that a number has an equal probability of being below and above 0.5.

We also point out that the time-averaged energy obtained from MD accounts for some entropy effect and therefore better represents the finite-temperature equilibrium than the global minimum energy obtained from MS. First, MD can overcome energy barriers, so it more effectively approaches the equilibrium state than MS. The average energy of a vibrational energy spectrum for the equilibrium structure is also exactly the energy measured from finite-time experiments. Contrarily, the minimum energy state may not occur in reality if it is associated with a small entropy. On the other hand, there is really no global energy minimization scheme. If such a scheme exists, grain boundaries would disappear after MS simulation which may not be desired.

VI. DISLOCATION CORE ENERGY CALCULATIONS

We have generated 184 dislocation energies, using MD, at a variety of dislocation spacings d and S and dislocation character angles β. By fitting the MD energies to Eqs. (1) – (12), we can determine elastic constants G and ν as well as 22 core energies E_c at 22 character angles using a chosen core radius $r_0 = 0.2$ Å and a stacking fault energy $\gamma_{sf} = 0.0085$ eV/Å^2. First, G and ν values are guessed. The stacking fault widths, λ, are then solved from the minimum energy (or equivalent force balance) condition [22]. Based on these λ, Eq. (1) is fitted to the MD data yielding 22 core energies and new G and ν. The new G and ν values are then used to recalculate λ, and Eq. (1) is refitted. This process is iterated until all the fitted parameters no longer change with further fitting; the results are summarized in Table I. The continuum lines and shaded regions in Fig. 4 and the data in Fig. 5 were obtained using these optimal parameters. These

continuum calculations provide quantitative information on the fraction of dissociation energy, ΔE_{dis}, over the total dislocation energy as shown in Fig. 4.

Table I. Fitted dislocation core energies E_c (eV/Å) for various dislocation character angles β (°) at fitted elastic constants G = 0.2085 (eV/Å^3), ν = 0.289, chosen core radius r_0 = 0.2 Å, and known stacking fault energy γ_{sf} = 0.0085 (eV/Å^2).

β	0.00	6.59	8.95	10.89	19.11	21.05	23.41	30.00	36.59	38.95	40.89
E_c	-0.418	-0.268	-0.260	-0.260	-0.250	-0.240	-0.240	-0.230	-0.220	-0.211	-0.215
β	49.11	51.05	53.41	60.00	66.59	68.95	70.89	79.11	81.05	83.41	90.00
E_c	-0.209	-0.207	-0.209	-0.209	-0.203	-0.210	-0.210	-0.211	-0.221	-0.211	-0.201

To develop an analytical expression for dislocation core energy as a function of character angle β, we assume that the core energy can be written as a polynomial Sinoidal function:

$$E_c(\beta) = \sum_{i=0}^{5} c_i sin^i \beta \quad (13)$$

where $c_0 - c_5$ are parameters. Fitting the data in Table I to Eq. (13), the parameters $c_0 - c_5$ were determined as shown in Table II. The dislocation core energies listed in Table I are also shown (using blue circles) in Fig. 6, where lines are calculated from Eq. (13). For comparison, the core energies were also fitted to Eq. (1) without considering dislocation dissociation (i.e., setting ΔE_{dis} = 0). These non-dissociated dislocation core energies are included (using red circles) in Fig. 6. Fig. 6 reveals that core energy is accurately represented by Eq. (13). An overall trend is that core energy increases with character angle, but the increase is most significant between 0° and 10°.

Table II. Parameters for dislocation core energy (eV/Å).

c_0	c_1	c_2	c_3	c_4	c_5
-0.268979	1.449739	-4.214258	5.158294	-2.247137	-2.247137

We point out that if using the same core radius, the non-dissociated dislocation core energies calculated here are very close to those reported in our previous work [15] for regular character angles (e.g., 0°, 30°, 60°, and 90°). There are slight differences between our current and

previous results for some non-regular character angles. This problem will be further explored below.

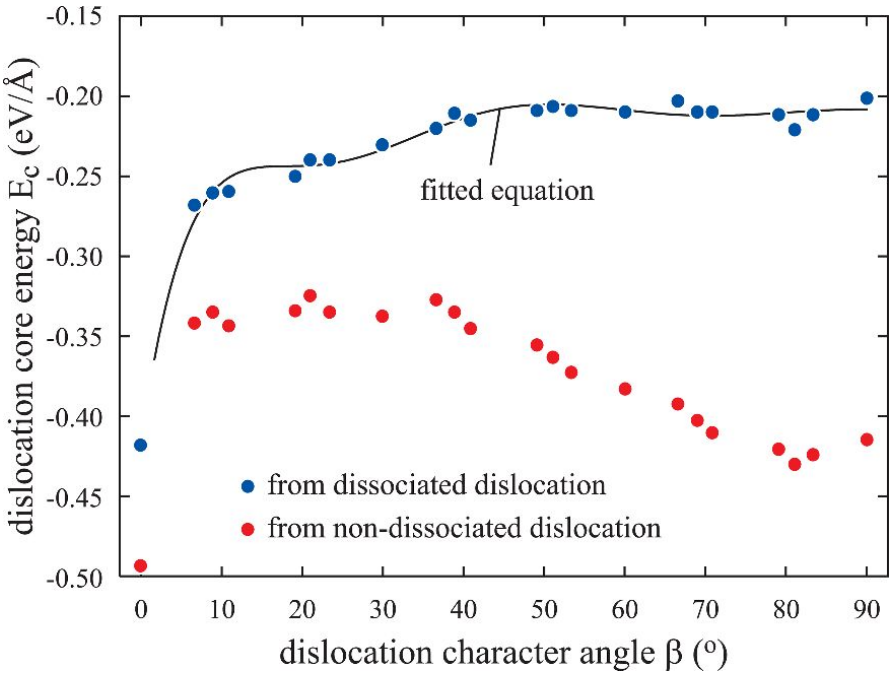

Fig. 6. Dislocation core energies as a function of dislocation character angle β.

VII. VALIDATION OF STACKING FAULT WIDTH

The MD dislocation energies also gave rise to 184 equilibrium stacking fault widths (λ) that minimize the energy. λ can also be measured from atomic configurations; although, the approach to measure the width can be highly subjective. We feel that the least subjective approach is to measure the number of (hexagonally-closely-packed) hcp atoms, which was done using OVITO visualization software [26,27]. Note, that the stacking fault width linearly increases with the number of hcp atoms (N_{hcp}) between unit length of partial dislocations. The N_{hcp} values obtained were linearly fitted to our calculated λ; the fitted results are plotted against calculated stacking fault width λ in Fig. 7(a). Fig. 7(a) confirms a linear correlation between N_{hcp} and λ, further validating our MD results and continuum model.

To more clearly demonstrate the nature of the correlation shown in Fig. 7(a), we visualize two configurations near the slip plane of the dislocations, one with a relatively narrow stacking fault width observed from a screw dislocation as shown in Fig. 7(b), and one with a relatively wide stacking fault width observed from a 79.11° dislocation as shown in Fig. 7(c). The energy minimum stacking fault width is predicted to be $\lambda = 4.2$ Å for the former case and $\lambda = 8.4$ Å for the latter case. Consistently, Figs. 7(b) and 7(c) show that the stacking fault width in the 79.11° dislocation is about twice of that in the screw dislocation case visually, albeit OVITO characterizes the dislocation in the screw dislocation case as a [110]/2 perfect dislocation as opposed to the two [112]/6 partial dislocation in the 79.11° case.

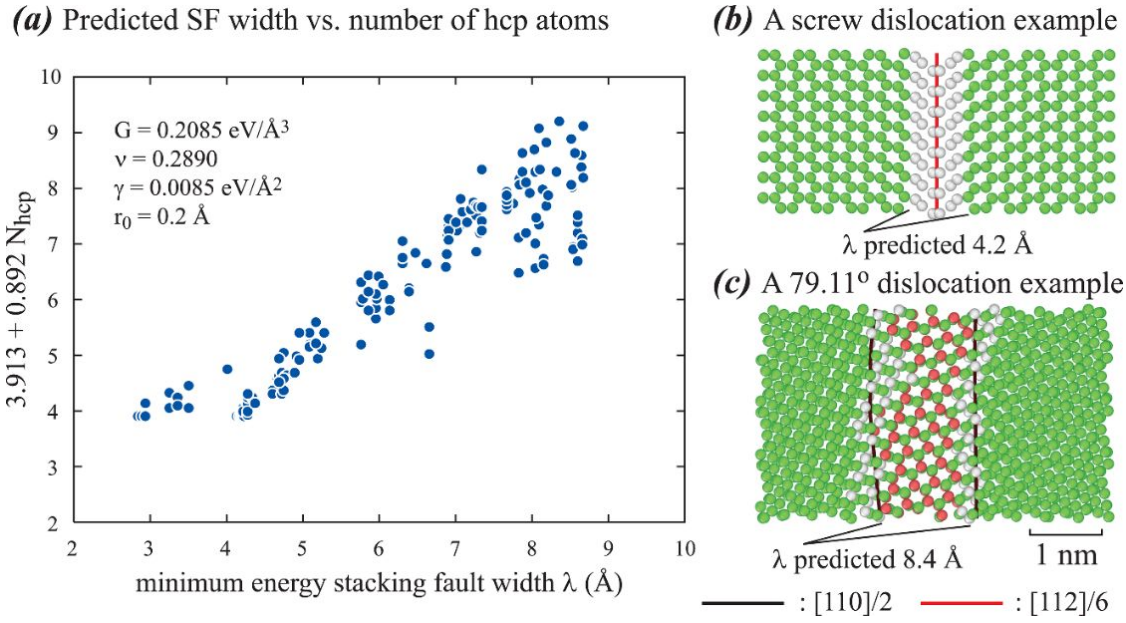

Fig. 7. Validation of stacking fault width calculations: (a) correlation between minimum energy stacking fault width and number of hcp atoms (N_{hcp}) between unit length of dislocations, (b) an example configuration of a short stacking fault width obtained from a screw dislocation (S ~ 94 Å, $L_y = 2d \sim 1220$ Å), and (c) an example configuration of a long stacking fault width obtained from a $\beta = 79.11°$ dislocation (S ~ 156 Å, $L_y = 2d \sim 407$ Å). The stacking fault width calculated from the minimum energy condition is noted in (b) and (c).

VIII. CRITICAL SIZE EFFECT

As stated above, the core energies derived from the current work are slightly higher than the ones obtained previously [15] for non-regular character angles. We note that in the previous work, all dislocation spacings S were above 29 Å for the regular angles but some of them fell below 20 Å for the non-regular angles. In the present work, all spacing S are above 40 Å. This suggests that there might be a critical size which impacts the calculated core energies. To explore the size effect, additional MD simulations were performed to calculate the energies for 60° dislocations with a fixed vertical dislocation spacing of $d = L_y/2 \sim 203.5$ Å and various smaller horizontal dislocation spacings S. The results, along with those obtained for larger S, are shown as the blue circles in Fig. 8(a). It is seen that when S > 25 Å, all data points fall on the continuum line despite not including the data for S < 43 Å in the continuum fitting; this strongly validates a constant core energy. When S approaches 20 Å, the dislocation energy suddenly drops, suggesting that dislocation core energy is altered. To ensure that this is not an artefact of the interatomic potential, we repeated the calculations using a literature embedded atom method potential for Al [28], and the results are included in Fig. 8(a) using red circles. Similar sudden drop of dislocation energy is observed when dislocation spacing S falls below 30 Å. Hence, the size-effect is likely a general phenomenon regardless of the potential.

To explore the origin of the sudden drop of energies at small dimensions, we show dislocation morphologies (generated using OVITO) for a small (S ~ 20 Å) and a larger (S ~ 43 Å) size system in Figs. 8(b) and 8(c) respectively. It can be seen that the larges system contains two partials; whereas, the smaller system exhibits a complex dislocation network. The formation of this network significantly reduces the energy of the system, as seen in Fig. 8(a). This observation indicates that opposite dislocations cannot stay intact when they are too close as elastic energy will drive a transformation. It also means that core energies can only be correctly

calculated when dislocation spacings S are above a threshold. Note, this size-effect was revealed using MD simulations; however, it is unclear if this phenomenon can be revealed by using MS where the system is more likely to be trapped in a local energy minimum.

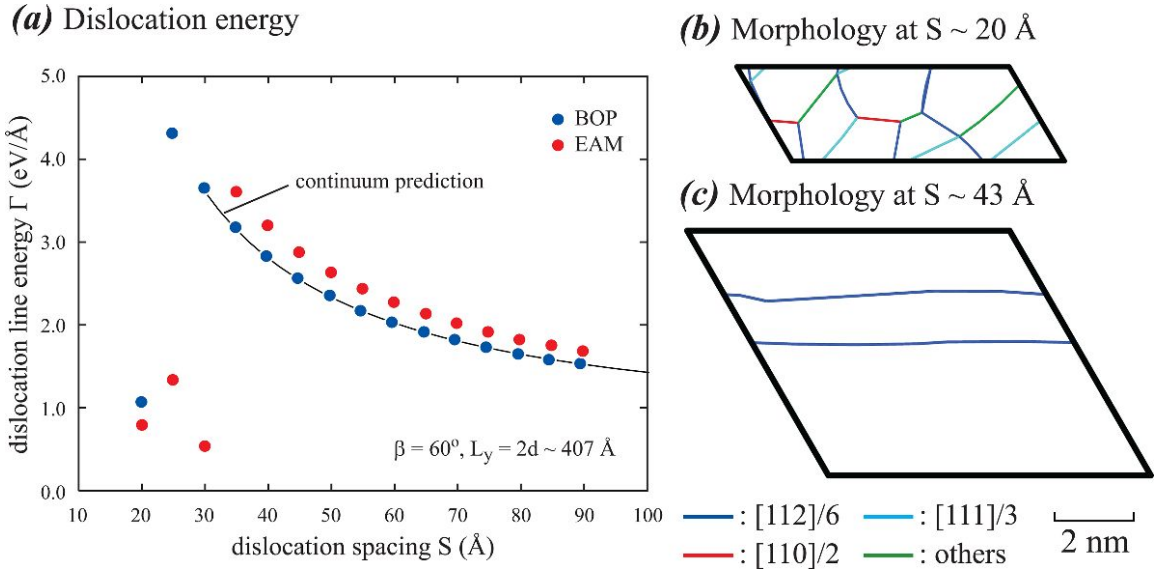

Fig. 8. Size effects on 60° dislocation simulations: (a) dislocation energies in a wide range of spacing S, (b) dislocation morphology at a small size S ~ 20 Å, and (c) dislocation morphology at a large size S ~ 43 Å.

The finding of a minimum spacing for dislocation core energy calculations is significant because most literature calculations employ small dimensions. The use of large system dimensions in molecular statics simulations, however, leads to unacceptably large errors [21]. This is not an issue for time-averaged MD simulations.

IX. CONCLUSIONS

A robust MD model has been developed to calculate core energy of dissociated dislocation at any character angle and spacing using only one dislocation dipole per computational cell. Significant computing resources have been used to achieve numerous physical understandings regarding dislocation core energies. First, time-averaged MD simulations can eliminate errors for

large computational systems and produce more relevant results to continuum models or experimental measurements. Second, the core energy of dissociated dislocations can be well descried by a polynomial Sinoidal function of dislocation character angle. Moreover, dislocation core energy is found to rapidly increase with character angle from 0^o to 10^o and then gradually increase until 90^o. Third, the dissociation energy can be non-negligible for some geometric conditions. Finally, there exists a critical dimension below which dislocation core energy cannot be correctly calculated due to the formation of a dislocation network.

X. CONFLICTS OF INTEREST

There are no conflicts of interest to declare.

XI. ACKNOWLEDGEMENTS

Sandia National Laboratories is a multi-mission laboratory managed and operated by National Technology and Engineering Solutions of Sandia, LLC., a wholly owned subsidiary of Honeywell International, Inc., for the U.S. Department of Energy's National Nuclear Security Administration under contract DE-NA-0003525. The authors gratefully acknowledge research support from the U.S. Department of Energy, Office of Energy Efficiency and Renewable Energy, Hydrogen and Fuel Cell Technologies Office. The views expressed in the article do not necessarily represent the views of the U.S. Department of Energy or the United States Government.

References

1 V. V. Bulatov, and W. Cai, *Computer Simulations of Dislocations* (Oxford University Press, London, 2006).
2 M. Heggie, R. Jones, A. Umerski, Interaction of Impurities with Dislocation Cores in Silicon, Philos. Mag. A 63 (1991) 571-584.
3 R. Jones, A. Umerski, P. Sitch, M. I. Heggie, A. Öberg, First-Principles Calculations of Dislocations in Semiconductors, Phys. Status Solidi A 137 (1993) 389-399.

4 N. Lehto, S. Öberg, Effects of Dislocation Interactions: Application to the Period-Doubled Core of the 90° Partial in Silicon, Phys. Rev. Lett. 80 (1998) 5568-5571.
5 A. S. Nandedkar, J. Narayan, Atomic Structure of Dislocations in Silicon, Germanium and Diamond, Philos. Mag. A 61 (1990) 873-891.
6 U. Trinczek, H. Teichler, Line Energies of 30°- and 90°-Partial Dislocations in Silicon and Germanium, Phys. Status Solidi A 137 (1993) 577-589.
7 W. Cai, V. V. Bulatov, J. Chang, J. Li, S. Yip, Periodic Image Effects in Dislocation Modelling, Phil. Mag. 83 (2003) 539-567.
8 W. Cai, V. V. Bulatov, J. Chang, J. Li, S. Yip, Anisotropic Elastic Interactions of a Periodic Dislocation Array, Phys. Rev. Lett. 86 (2001) 5727-5730.
9 J. Li, C. Z. Wang, J. P. Chang, W. Cai, V. V. Bulatov, K. M. Ho, S. Yip, Core Energy and Peierls Stress of a Screw Dislocation in BCC Molybdenum: A Periodic-Cell Tight-Binding Study, Phys. Rev. B 70 (2004) 104113-8.
10 J. R. K. Bigger, D. A. McInnes, A. P. Sutton, M. C. Payne, I. Stich, R. D. King-Smith, D. M. Bird, L. J. Clarke, Atomic and Electronic Structures of the 90° Partial Dislocation in Silicon, Phys. Rev. Lett. 69 (1992) 2224-2227.
11 S. Ismail-Beigi, T. A. Arias, Ab Initio Study of Screw Dislocations in Mo and Ta: A New Picture of Plasticity in BCC Transition Metals, Phys. Rev. Lett. 84 (2000) 1499-1502.
12 G. Wang, A. Strachan, T. Cagin, W. A. Goddard III, Role of Core Polarization Curvature of Screw Dislocations in Determining the Peierls Stress in BCC Ta: A Criterion for Designing High-Performance Materials, Phys. Rev. B 67 (2003) R140101-4.
13 J. Bennetto, R. W. Nunes, D. Vanderbilt, Period-Doubled Structure for the 90° Partial Dislocation in Silicon, Phys. Rev. Lett. 79 (1997) 245-248.
14 X. Blase, K. Lin, A. Canning, S. G. Louie, D. C. Chrzan, Structure and Energy of the 90° Partial Dislocation in Diamond: A Combined Ab Initio and Elasticity Theory Analysis, Phys. Rev. Lett. 84 (2000) 5780-5783.
15 X. W. Zhou, R. B. Sills, D. K. Ward, R. A. Karnesky, Atomistic Calculations of Dislocation Core Energy in Aluminium, Phys. Rev. B 95 (2017) 054112-8.
16 X. W. Zhou, D. K. Ward, J. A. Zimmerman, J. L. Cruz-Campa, D. Zubia, J. E. Martin, F. van Swol, An Atomistically Validated Continuum Model for Strain Relaxation and Misfit Dislocation Formation, J. Mech. Phys. Sol. 91 (2016) 265-277.
17 P. J. Gibbs, P. D. Hough, K. Thurmer, B. P. Somerday, C. San Marchi, and J. A. Zimmerman, Stacking fault energy based alloy screening for hydrogen compatibility, JOM, 72 (2020) 1982-1992.
18 X. W. Zhou, D. K. Ward, M. E. Foster, An Analytical Bond-order Potential for the Aluminum Copper Binary System, J. Alloys Comp. 680 (2016) 752-767.
19 W. P. Kuykendall, W. Cai, Conditional Convergence in Two-Dimensional Dislocation Dynamics, Modelling. Simul. Mater. Sci. Eng. 21 (2013) 055003-17.
20 S. Pattamatta, R. S. Elliott, E. B. Tadmor, Mapping the Stochastic Response of Nanostructures, PNAS 111 (2014) E1678-1686.
21 X. W. Zhou, and S. M. Foiles, Ed. J. P. Hessling, *Uncertainty Quantification and Model Calibration* (INTECH, Rijeka, Croatia, 2017).
22 X. W. Zhou, Thermodynamic Analysis of Dissociation of Periodic Dislocation Dipoles in Isotropic Crystals, RSC Adv. 10 (2020) 35062-35071.
23 LAMMPS download site: lammps.sandia.gov.

24 S. Plimpton, Fast Parallel Algorithms for Short-Range Molecular Dynamics, J. Comp. Phys. 117 (1995) 1-19.
25 Supplemental material ....
26 A. Stukowski, V. V. Bulatov, A. Arsenlis, Automated Identification and Indexing of Dislocations in Crystal Interfaces, Modelling Simul. Mater. Sci. Eng. 20 (2012) 85007-16.
27 A. Stukowski, Visualization and Analysis of Atomistic Simulation Data with OVITO – the Open Visualization Tool, Modelling Simul. Mater. Sci. Eng. 18 (2010) 15012-7.
28 M. I. Mendelev, M. J. Kramer, C. A. Becker, M. Asta, Analysis of Semi-Empirical Interatomic Potentials Appropriate for Simulation of Crystalline and Liquid Al and Cu, Philos. Mag. 88 (2008) 1723-1750.